CHAPTER 7

EFFECT OF ka_{eff} VALUES AND FREQUENCY RANGE USED IN ESTIMATION

While performing the analysis of the different signal processing techniques discussed in Chapter 6, it was noted that the precision of estimates from the basic Spectral Fit algorithm were better for the larger scatterer size of 45 μm. For example, the smallest percent deviation of scatterer size (precision) in Figure 6.12 is ~40% for the 25 μm scatterers, whereas the percent deviation at the same window length in Figure 6.13 is ~15% for the 45 μm scatterers. This calls into question the previous choice of ka_{eff} values that attempted to center the bandwidth near a ka_{eff} value of 0.8 (i.e., a frequency of 8 MHz for a scatterer size of 25 μm). Initially, this ka_{eff} value had been selected because the optimal range for ka_{eff} values had been previously reported as being from 0.5 to 1.2 [*Insana and Hall*, 1990]. Hence, in this chapter the impact the choice of ka_{eff} values has on the estimation scheme is analyzed. The analysis is done for both the Spectral Fit algorithm that estimates both scatterer size and total attenuation as well as for the traditional minimization algorithm that assumes the attenuation is already known. The analysis only considers scatterers with Gaussian impedance distributions.

7.1 ka_{eff} Range Results for the Spectral Fit Algorithm

In order to evaluate the impact the ka_{eff} values have on the Spectral Fit algorithm, many different sets of simulations were performed. In the simulations, a weakly focused $f/4$ transducer with a focal length of 5 cm was once again used to sonify an infinite half-space with scatterers placed at a density of 35/mm^3. Also, 1000 independent scatterer distributions were used for each of the simulated cases, and a waveform was generated for each distribution. A sampling frequency of 53 MHz was used when "digitizing" each of the waveforms. The resulting 1000 independent waveforms were combined into 40 sets with 25 waveforms per set. The 25 waveforms in each set were windowed with a hamming window whose length varied from 1 to 8

mm and averaged in the normal spectral domain. The averaged spectrum was then compensated for windowing and used in the Spectral Fit algorithm to obtain an estimate for total attenuation α and effective scatterer size a_{eff}. The effect of using different ka_{eff} ranges was evaluated by varying the attenuation of the half-space, the scatterer size, the bandwidth of the source, and the amount of electronic noise added to the simulated waveforms before processing.

7.1.1 Results for different source bandwidths

The first case that will be analyzed involved varying the bandwidth of the source and the scatterer size while maintaining the same value for the half-space attenuation. In order to facilitate the analysis, the attenuation selected for the half-space was 0 dB/cm/MHz, so that the attenuation would not cause any downshift in the backscattered spectrum. However, the Spectral Fit algorithm still solved for the attenuation as if it was unknown. The bandwidth of the source was varied by changing the bandwidth of the Rayleigh distribution of the filtering characteristics for the source (i.e., H(f)). In the simulations, H(f) was given by

$$H(f) = \frac{|f| \cdot \exp\left(-\left(\frac{f - f_R}{\sigma_R}\right)^2\right)}{\max_{\forall f}\left(f \cdot \exp\left(-\left(\frac{f - f_R}{\sigma_R}\right)^2\right)\right)}, \tag{7.1}$$

where f_R was 8 MHz and σ_R was varied as 2, 4, and 6 MHz in order to change the bandwidth of the source. Then, the frequency range (i.e., range of ka_{eff} values) used in the minimization routine was given by the set of all frequencies corresponding to signal levels greater than

$$N_{Floor} = \max\left(\left[-20 \quad \text{mean}\left(10\log\left(\frac{P_{scat}\left(f_{N-200} : f_N\right)}{\max_{\forall f}\left(\left\{P_{scat}(f)\right\}_{\substack{Gaussian \\ fit}}\right)}\right)\right) + 6\right]\right) \tag{7.2}$$

as was discussed in Chapter 5. For each source bandwidth, simulations were performed with scatterer effective radii varying from 5 to 105 μm. However, within each simulation, every scatterer had the same size.

The results at each bandwidth for a window length of 3 mm for all of the scatterer sizes are shown in Figure 7.1. There is a significant degradation in both accuracy and precision for the

estimates at the same scatterer size using the smaller source bandwidths. In addition, the precision (Figure 7.1b) and accuracy (Figure 7.1a) of the size estimates improves with increasing scatterer size indicating a dependence on the range of ka_{eff} values used in the minimization routine. However, the precision (Figure 7.1d) of the total attenuation estimates degrades slightly with increasing scatterer size. Because it was shown in Chapter 4 that increases in scatterer size slightly reduce the bandwidth, the precision of the total attenuation estimate might only depend on the frequency range used in the minimization routine.

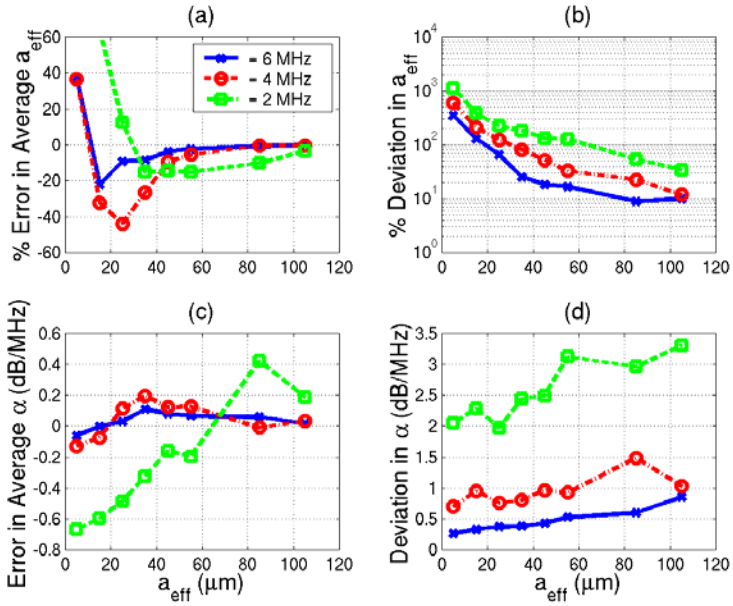

Figure 7.1: Simulation results for different source bandwidths for (a) the percent error in the average scatterer size, (b) the percent deviation in the scatterer size, (c) the error in the average total attenuation, and (d) the deviation in the total attenuation for different scatterer sizes plotted versus scatterer size.

In order to validate the dependence of the size estimate on the range of ka_{eff} values and the dependence of the attenuation estimate on the range of frequencies, the results shown in Figure 7.1 were replotted in Figure 7.2 versus Δka_{eff} (maximum value of ka_{eff} minus minimum value of ka_{eff}) and frequency range (maximum frequency minus minimum frequency) for the size and attenuation estimates, respectively. The frequency range and Δka_{eff} range determined for Figure 7.2 was the ideal range given by the set of all frequencies for which

$$10\log\left(\frac{P_{ref}(f)e^{-0.827\left(ka_{eff}\right)^2}e^{-4\alpha_o f z_T}}{\max_f\left(P_{ref}(f)e^{-0.827\left(ka_{eff}\right)^2}e^{-4\alpha_o f z_T}\right)}\right) > -20\,\text{dB} \tag{7.3}$$

because for these simulated cases no noise had been added to the waveforms. Clearly from Figure 7.2, the accuracy (Figure 7.2a) and precision (Figure 7.2b) of the size estimates exhibit a strong and consistent dependence on Δka_{eff} as is indicated by the overlapping curves. Likewise, the accuracy (Figure 7.2c) and precision (Figure 7.2d) of the attenuation estimates exhibit a strong dependence on the frequency range used in the minimization. However, the relationship between the accuracy of the attenuation estimates and the frequency range used by the minimization is not as consistent (i.e., curves do not overlap) as the other cases shown in Figure 7.2.

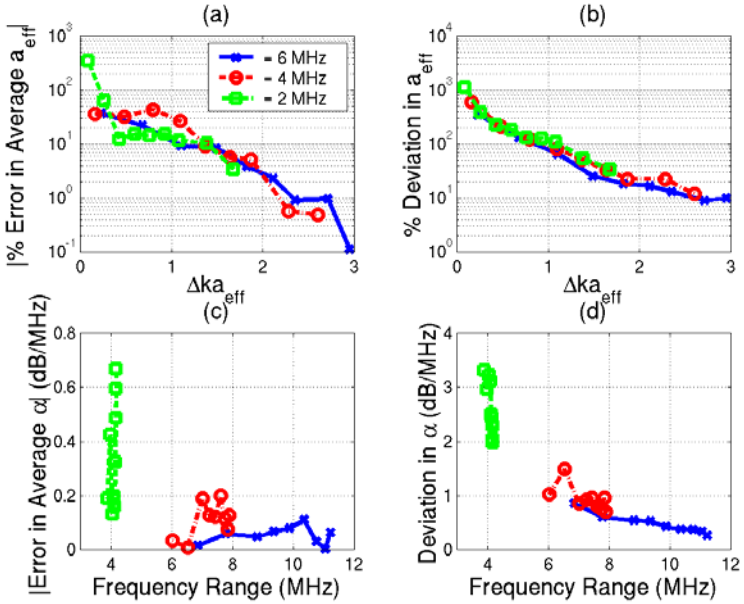

Figure 7.2: Simulation results for different source bandwidths for (a) the percent error in the average scatterer size, (b) the percent deviation in the scatterer size, (c) the error in the average total attenuation, and (d) the deviation in the total attenuation for different scatterer sizes plotted versus Δka_{eff} and frequency range used in minimization.

7.1.2 Results for different half-space attenuations

After showing that the accuracy and precision of the estimates were dependent on Δka_{eff} and the frequency range used when varying the bandwidth of the source, changes in the Δka_{eff} and the frequency range were investigated to determine if they could also explain the previously observed loss in precision with increasing attenuation (Chapter 5). Hence, simulations were performed for half-space attenuation of 0.3 dB/cm/MHz, 0.5 dB/cm/MHz, and 1 dB/cm/MHz. For each value of half-space attenuation, the bandwidth of the source was held constant and set by using a σ_R value of 6 MHz in Equation (7.1). The frequency range used in the minimization

routine, however, would still be decreased at large half-space attenuations by the corresponding down shift of the spectrum. In addition, the frequency range would also be decreased by increasing scatterer size. For the 0.3 dB/cm/MHz half-space attenuation, the simulation was repeated for scatterer sizes ranging from 5 μm to 75 μm. Likewise, for the 0.5 dB/cm/MHz and 1 dB/cm/MHz half-space attenuations, the scatterer sizes ranged from 5 μm to 85 μm and 5 μm to 150 μm, respectively. Every scatterer was the same size for any given simulation.

The scatterers once again had Gaussian impedance distributions and were placed at a density of 35/mm^3. One thousand independent scatterer distributions were generated, grouped into 40 sets of 25 waveforms, windowed with a hamming window (length varied from 1 to 8 mm), and then averaged in the normal spectral domain. The convolution effects of windowing were compensated, and the frequency range used in the minimization routine for the Spectral Fit algorithm was given by Equation (7.2).

The results for the different scatterer sizes and attenuations for a hamming window length of 3 mm are shown in Figure 7.3. In addition to the three half-space attenuation cases just described, we have also included in the plot the half-space attenuation of 0 dB/cm/MHz at a σ_R value of 6 MHz from Section 7.1.1 as well as the results obtained for half-space attenuations of 0 to 1 dB/cm/MHz for a scatterer size of 25 μm that had been used to evaluate the basic Spectral Fit algorithm in Chapter 5. However, this time the signals were averaged in the normal spectral domain, the convolution effects of windowing were corrected, and the frequency range used in the minimization routine was given by Equation (7.2). Once again, the accuracy (Figure 7.3a) and precision (Figure 7.3b) of the size estimates exhibit a strong and consistent dependence on Δka_{eff} as is indicated by the overlapping curves. Likewise, the precision of the total attenuation estimate seems to exhibit a consistent dependence on the frequency range used to perform the minimization. Therefore, the degradation in estimator performance observed previously for larger attenuations was due entirely to a smaller Δka_{eff} and a smaller frequency range. Hence, the amount of attenuation of the half-space, taken independently, relative to the attenuation of the medium used to acquire the reference spectrum (i.e., 0 dB/cm/MHz for water surrounding rigid plate) does not effect the performance of the Spectral Fit algorithm.

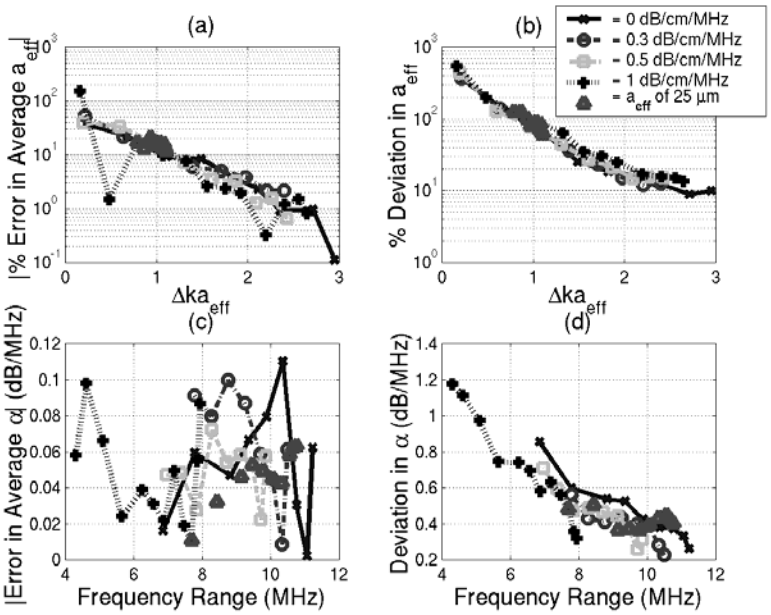

Figure 7.3: Simulation results for different half-space attenuations for (a) the percent error in the average scatterer size, (b) the percent deviation in the scatterer size, (c) the error in the average total attenuation, and (d) the deviation in the total attenuation plotted versus Δka_{eff} and the frequency range used in minimization.

To further demonstrate the lack of dependence of the algorithm on the attenuation of the half-space relative to the reference medium, a new reference waveform was acquired. This time, the attenuation of the medium between the source and reference plate placed at the focal plane was changed from 0 dB/cm/MHz (water) to 0.3 dB/cm/MHz. The new reference waveform was then used in the Spectral Fit algorithm to estimate total attenuation and scatterer size for a half-space with an attenuation of 0.3 dB/cm/MHz containing Gaussian scatterers with radii of 25 µm. The results for both the lossless (water) and lossy reference waveforms for this case are shown in Figure 7.4. The results for the two different reference waveforms are identical confirming that attenuation of the half-space relative to the reference does not matter.

7.1.3 Results for different levels of electronic noise

In Chapter 5, the performance of the Spectral Fit algorithm was also degraded by adding white "electronic" noise to the simulated waveforms in addition to the degradation observed by increasing the attenuation of the half-space. Hence, after completing the investigation on the impact of attenuation discussed in Section 7.1.2, the impact of adding white, Gaussian distributed, noise to the acquired waveforms was investigated. The waveforms selected for the

investigation were from the earlier simulation study (Section 7.1.1) for a half-space attenuation of 0 dB/cm/MHz, an σ_R of 6 MHz, and a scatterer effective radius of 105 μm. The amount of noise added to the waveforms was set by specifying the noise power relative to the signal backscattered from the reference plate placed at the focal plane in a water bath so that all 1000 of the generated waveforms would receive the same amount of additive noise. The noise power was varied in a series of simulations so that the mean value of *SNR*, calculated according to Equation (4.20), varied from 36 to 3 dB.

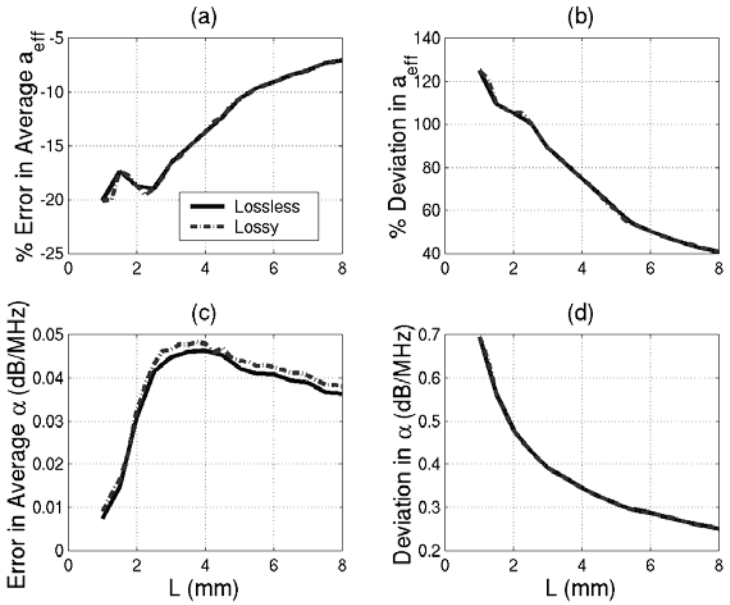

Figure 7.4: Simulation results when the reference medium has an attenuation of 0.3 dB/cm/MHz (lossy) and 0 dB/cm/MHz (loss less) showing (a) the percent error in the average scatterer size, (b) the percent deviation in the scatterer size, (c) the error in the average total attenuation, and (d) the deviation in the total attenuation plotted versus window length for a half-space with an attenuation of 0.3 dB/cm/MHz containing 25 μm scatterers.

The results for all of the different noise levels at a hamming window length of 3 mm are shown in Figure 7.5. Also, the results without any noise for σ_R values of 2 MHz, 4 MHz, and 6 MHz at an attenuation of 0 dB/cm/MHz from Figure 7.2 and the results for an attenuation of 1 dB/cm/MHz from Figure 7.3 are replotted in Figure 7.5 for the sake of comparison. Once again, the accuracy and precision of the scatterer size estimate for the noisy signals has the same dependence on Δka_{eff} that was observed in the earlier simulations (Figure 7.5a and 7.5b). Similarly, the accuracy and precision of the total attenuation estimate also appear to have the same dependence on the frequency range that was observed in the earlier simulations shown in

Figure 7.2 that varied the value of σ_R. However, the precision of the attenuation estimate for the half-space attenuation of 1 dB/cm/MHz at smaller frequency ranges (i.e., less than 6 MHz) appears to be better than that expected by the other simulations. This difference was not noticed previously because of the gap in data for the frequency range from 4 to 6 MHz. From this we can conclude that although the accuracy and precision of the attenuation estimate are improved with increasing frequency range used to obtain the estimate, the exact amount of improvement may be difficult to predict from the frequency range alone.

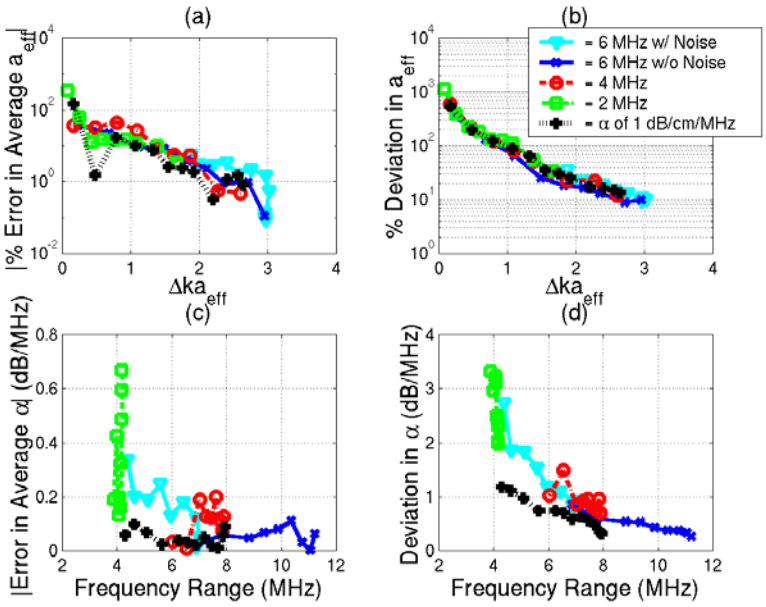

Figure 7.5: Simulation results for different levels of electronic noise for (a) the percent error in the average scatterer size, (b) the percent deviation in the scatterer size, (c) the error in the average total attenuation, and (d) the deviation in the total attenuation plotted along with results for different bandwidth sources and a half-space attenuation of 1 dB/cm/MHz versus Δka_{eff} and the frequency range used in minimization.

7.2 ka_{eff} Range Results for the Traditional Algorithm

In the previous section, it was observed that the accuracy and precision of the size estimates were improved as we increased the size of the Δka_{eff} range used in the minimization routine. In this section, the traditional estimation scheme where the attenuation is known *a priori* was investigated to determine if the same trend in improvement was also found. The relationship between frequency range and precision of the size estimate using the traditional estimation scheme has been investigated briefly by other authors [*Chaturvedi and Insana*, 1996; *Wear*, 2001b]. However, in their analysis they only looked at the impact of frequency range and not the Δka_{eff} range. In addition, although Chaturvedi and Insana's results for two different

scatterer sizes suggest a consistent dependence of precision on the Δka_{eff} range, the results were not presented in a form to facilitate a comparison. Hence, the comparison was performed using new simulation results.

Before performing the comparison, however, the initial ka_{eff} values used in the estimate were investigated to determine if they should be greater than 0.5 as had been previously reported [*Insana and Hall*, 1990]. Hence, simulations were performed where the Δka_{eff} range was set to be one, and the initial ka_{eff} value was varied from 0.1 to 2. The frequency range used in the minimization was manually selected for these simulations, but care was still taken to insure that the selected frequencies corresponded to signal values greater than the noise floor of the simulated waveforms. The half-space used in the simulations had an attenuation of 0 dB/cm/MHz and once again contained Gaussian scatterers with an a_{eff} of 25 μm at a density of 35/mm^3. The sources used in the simulations had very large bandwidths that would not be physically realizable with a real source so that the large span of ka_{eff} values could be tested. The bandwidth was set by using a filtering function given by

$$H(f) = \frac{\left(1 - \exp\left(-\left|6\,\mathrm{MHz}^{-1} f\right|\right)\right) \cdot \exp\left(-\left(\frac{f}{20\,\mathrm{MHz}}\right)^2\right)}{\max_{\forall f}\left(\left(1 - \exp\left(-\left|6\,\mathrm{MHz}^{-1} f\right|\right)\right) \cdot \exp\left(-\left(\frac{f}{20\,\mathrm{MHz}}\right)^2\right)\right)} \tag{7.4}$$

while still shock exciting the simulated transducers (i.e., $V_{inc}(\omega)$=1). Three different sources were used in the simulations with f-numbers of 1, 2, and 4. The effects of focusing and attenuation were removed using the generalized attenuation-compensation function discussed in Chapter 2.

Once again, 1000 backscattered waveforms for 1000 independent scatterer distributions were generated and combined into 40 sets with 25 waveforms per set for each source. However, the sampling rate selected when "digitizing" the signal for the simulated waveforms was 125 MHz, not the 53 MHz used previously, in order to accommodate the large bandwidth of the transducer. Also, no "electronic" noise was added to the simulated waveforms. The 25 waveforms in each set were windowed with a hamming window of length 3 mm. The averaged spectrum was then compensated for windowing using the same compensation technique that was described in Chapter 5 for the Spectral Fit Algorithm.

The accuracy and precision results for all three sources for the different initial ka_{eff} values are shown in Figure 7.6. The precision of the size estimate for all of the sources appears to be approximately the same for initial ka_{eff} values between 0.5 and 2, and the precision of the estimates degrades significantly for smaller initial ka_{eff} values (Figure 7.6b). Likewise, the accuracy of the *f*/1 source follows a similar trend (Figure 7.6a). These results are in agreement with the lower limit of 0.5 reported by *Insana and Hall* [1990]. Because their upper limit of 1.2 resulted from using the approximate form factor for glass bead scatterers, no upper limit was expected in the results shown in Figure 7.6. From these results, we conclude that care should be taken to insure that the initial ka_{eff} value is always larger than 0.5 when making further assessments of the traditional algorithm.

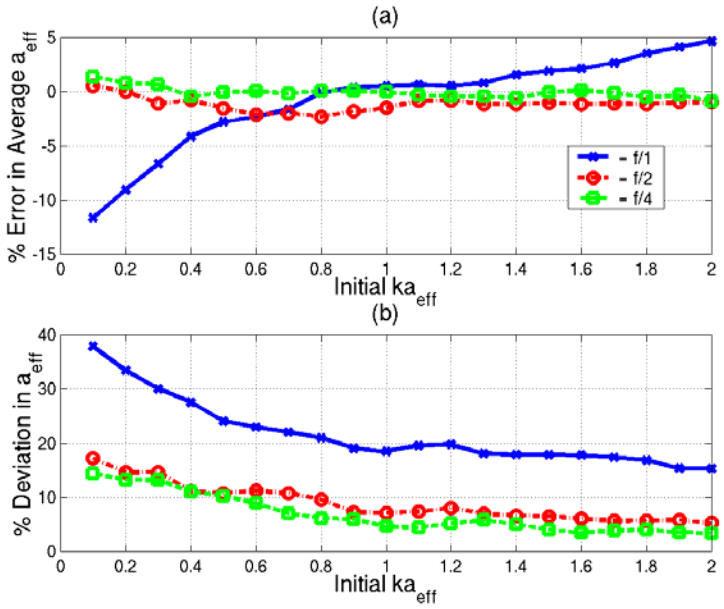

Figure 7.6: Simulation results for different initial ka_{eff} values from the traditional estimation algorithm (α known) for different f-number transducers showing (a) the percent error in the average scatterer size and (b) the percent deviation in the scatterer size.

Once the smallest acceptable value for ka_{eff} of 0.5 had been determined, the impact of the range of ka_{eff} values could be assessed. The assessment was done by reanalyzing the simulated waveforms discussed in this section by manually selecting the Δka_{eff} range from 0.25 to 2.5. For all of these ranges, the central ka_{eff} value was maintained at 1.75 to insure that the initial ka_{eff} was always greater than 0.5. The results for all three of the different f-number sources are shown in Figure 7.7. From Figure 7.7b, it is clear that increasing the Δka_{eff} range used in the traditional estimation algorithm results in a dramatic improvement in precision similar to that observed for

the Spectral Fit algorithm. However, the accuracy of the estimates (Figure 7.7a) does not appear to be significantly influenced by the Δka_{eff} range used in the traditional estimation algorithm. The overall precision and accuracy is much better in the traditional algorithm as compared to the Spectral Fit algorithm because the attenuation is known *a priori* for the traditional algorithm. Hence, the curves from the two algorithms can only be compared qualitatively.

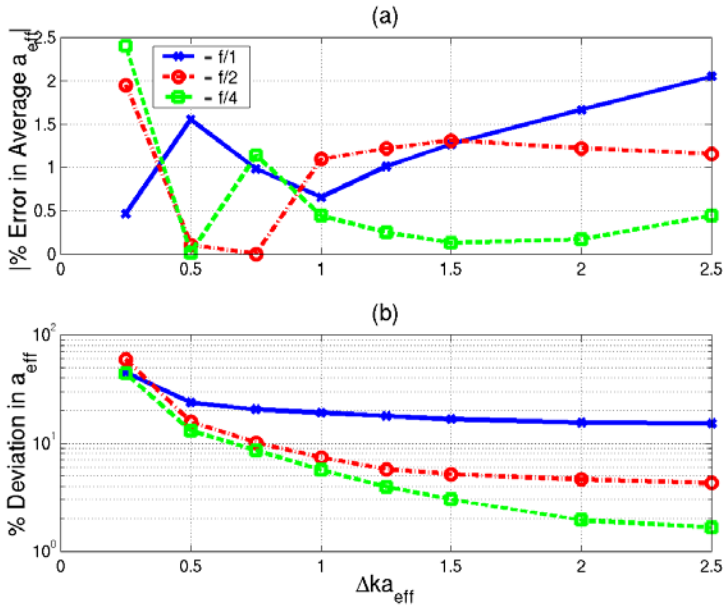

Figure 7.7: Simulation results for different Δka_{eff} ranges from the traditional estimation algorithm (α known) for different f-number transducers showing (a) the percent error in the average scatterer size and (b) the percent deviation in the scatterer size.

7.3 Initial ka_{eff} Results for the Spectral Fit Algorithm

In the previous assessment of the Spectral Fit algorithm, the dependence of the accuracy and precision of the scatterer size and attenuation estimates on the frequency range and Δka_{eff} values was determined by varying the bandwidth of the source, the scatterer size, the amount of "electronic" noise, and the attenuation of the half-space region. Regardless of these parameters, the largest reasonable frequency range was selected for the estimates based on Equation (7.2). As a result, the location of the frequencies (i.e., initial ka_{eff} value) to be used by the estimator was not precisely controlled although the overall range could be varied. After verifying that the initial value for ka_{eff} used in the traditional estimation scheme should be greater than 0.5, the Spectral Fit algorithm was investigated to determine if a similar lower limit existed. Hence, in this section a set of simulations is discussed where the initial and final values of ka_{eff} were manually selected so that the location of the Δka_{eff} could be precisely varied for the Spectral Fit

algorithm. However, care was still taken to insure that the frequency range used in the minimization did not extend into spectral regions dominated by noise.

In order to vary the location of the Δka_{eff} while still maintaining a Δka_{eff} that would yield reasonable accuracy and precision, an ultrasound source with a very large frequency bandwidth was desired. Hence, simulations were performed using a source with a σ_R of 18 MHz and a f_R of 8 MHz in the filtering function given by Equation (7.1). It is not possible using current technology to obtain a real source with this large a bandwidth. However, a bandwidth of this duration was required for the analysis. The source had an f-number of 4 and a 5 cm focal length as well.

The idealized source sonified a half-space containing scatterers with Gaussian impedance distributions with effective radii of 25 μm at a density of 35/mm^3. The half-space had an attenuation of 0 dB/cm/MHz. Once again, 1000 backscattered waveforms for 1000 independent scatterer distributions were generated and combined into 40 sets with 25 waveforms per set. However, the sampling rate selected when "digitizing" the signal for the simulated waveforms was 160 MHz instead of the 53 MHz used previously in order to accommodate the large bandwidth of the transducer. Also, no "electronic" noise was added to the simulated waveforms. The 25 waveforms in each set were windowed with a hamming window with a length of 3 mm and averaged in the normal spectral domain. The averaged spectrum was then compensated for windowing and used in the Spectral Fit algorithm to obtain an estimate for total attenuation and effective scatterer size.

In addition to the idealized source just described, the simulated *f*/4 data used previously to assesses the impact of the ka_{eff} values on the performance of the traditional algorithm (i.e., source filtering function given by Equation (7.4)) was also reanalyzed using the Spectral Fit algorithm. For both idealized sources, Δka_{eff} was set to one and the initial ka_{eff} value was varied over the largest possible range while still avoiding the sections of the spectrum dominated by noise. Because the scatterer size, attenuation, frequency range used in the minimization, and focal length for both of these simulated sources were identical, the accuracy and precision for both idealized sources should have been the same. However, this was not the case as is shown in Figure 7.8.

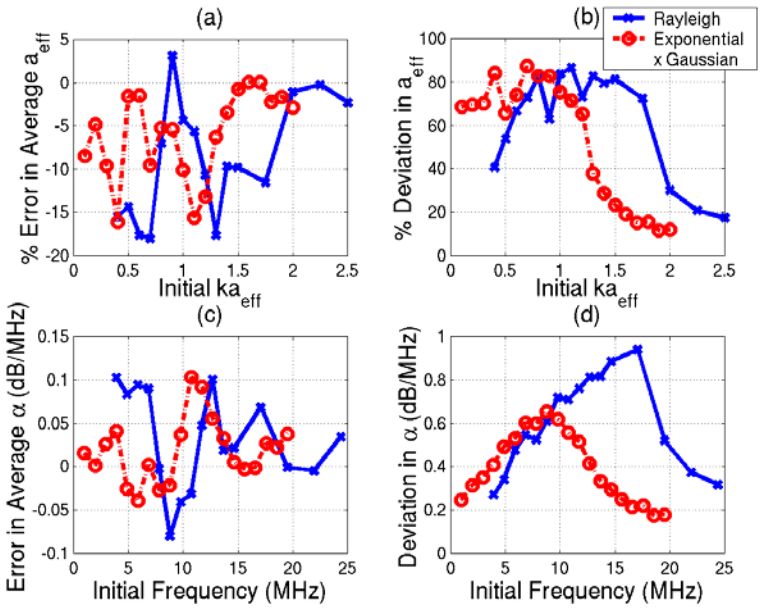

Figure 7.8: Simulation results for different source filtering functions $H(f)$ for (a) the percent error in the average scatterer size, (b) the percent deviation in the scatterer size, (c) the error in the average total attenuation, and (d) the deviation in the total attenuation plotted versus the initial ka_{eff} value and the initial frequency used in minimization for a Δka_{eff} of 1.

Begin by considering the precision results for the attenuation estimate shown in Figure 7.8d. For both sources, the precision initially degrades with increasing initial frequency, peaks, and then improves as the initial frequency continues to increase. Hence, the improved precision for the attenuation estimate for a half-space attenuation of 1 dB/cm/MHz as compared to 0 dB/cm/MHz for the same frequency range shown in Figure 7.5 may be due to the smaller initial frequency used in the estimate due to the shifting of the spectrum to lower frequencies by the attenuation. However, the location of the peak is different for the two different sources. Hence the source whose filtering function is given by Equation (7.4) has better precision at smaller values of the initial frequency.

Likewise, the precision of the scatterer size estimate (Figure 7.8b) appears to degrade slightly for small values of the initial ka_{eff} value as the initial ka_{eff} value is increased, plateau at a constant value, and then exhibit dramatic improvement in precision for larger initial ka_{eff} values. Once again, the onset of the dramatic improvement in precision for the size estimate is different for the two sources and corresponds to the improvement observed in the precision of the attenuation estimate. The improvement in precision for both estimates also appears to correlate with a slight improvement in the accuracy of the estimates (Figures 7.8a and 7.8c), although in

general the accuracy of the estimates does not appear to be strongly affected by the initial ka_{eff} or frequency value.

The fact that the deviation of the estimates for the two different sources peak at different locations is very puzzling. All of the previous theory predicted that once the backscattered spectrum was divided by the reference spectrum and an appropriate range of frequencies was selected for the minimization, the frequency response of the source would not affect the estimates [*Lizzi et al.*, 1997b; *Chaturvedi and Insana*, 1996; *Wear*, 2001b; *Insana et al.*, 1990]. Therefore, the first goal was to determine if the difference in the peaking was a simulation artifact that would not be present in signals from real tissue. One possibility is that the peaking results from having too few scatterers per resolution cell because the transmitted pulse for the Rayleigh spectrum (i.e., Equation (7.1)) had larger support in the time domain by approximately a factor of 2. As a result, the Rayleigh spectrum would always have more scatterers per resolution cell and would subsequently peak at a higher value for the initial frequency if the peaking were related to the number of scatterers per resolution cell.

In order to test this possibility, more simulations were performed using the source with the filtering function given by Equation (7.4). The scatterer size, half-space attenuation, and Δka_{eff} range used in the minimization routine were identical to the results presented in Figure 7.8. The only difference was that the scatterer number density was increased from 35/mm^3 to 70/mm^3. If the hypothesis relating the peaking to the scatterer number density was correct, then the peak in the deviation should be shifted to higher values of the initial frequency in these simulations. The results for the higher number density are shown with the results for the original number density in Figure 7.9. The results for the two different number densities are indistinguishable. Hence, the peak in the deviation is not related to the number of scatterers per resolution cell.

To further explore the observed improvement in precision with increasing initial frequency, more simulations were performed using a scatterer size of 50 μm instead of 25 μm. Once again, the simulations were performed using the source with the filtering function given by Equation (7.4) and a lossless half-space with scatterers positioned at a density of 35/mm^3. The hamming window used to gate out the region of interest also had a length of 3 mm. Because the scatterer size was larger, there were two reasonable choices for the size of the Δka_{eff} range used in the minimization routine. A Δka_{eff}=1 could be selected, as was done in the other simulations

resulting in a smaller overall frequency range to be used in the estimate, or a Δka_{eff} =2 could be selected, which would use the same size frequency range as had been used for the smaller scatterer size estimates. In the simulations, both possibilities were considered while using the widest range of initial ka_{eff} values. The results for the simulations are shown in Figure 7.10 along with the previous results for the 25 μm scatterer using the filtering function given by Equation (7.4). Plots (a) and (c) show the exact deviation in the scatterer size and attenuation estimates, whereas plots (b) and (d) show the deviation normalized with respect to the largest value of the deviation. The normalization was done so that the results for the different Δka_{eff} values could be compared on the same graph.

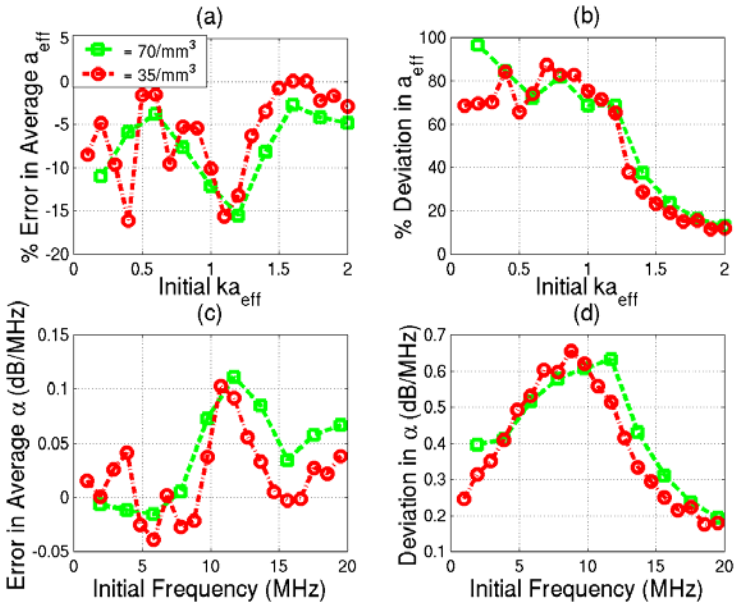

Figure 7.9: Simulation results for different scatterer number densities for (a) the percent error in the average scatterer size, (b) the percent deviation in the scatterer size, (c) the error in the average total attenuation, and (d) the deviation in the total attenuation plotted versus the initial ka_{eff} value and the initial frequency used in minimization for a Δka_{eff} of 1.

From these curves, it is clear that the Δka_{eff} value or total frequency range does not influence the location of the deviation peak because the peak occurs at the same location for both Δka_{eff} values. Furthermore, it appears that it is the initial frequency used in the minimization as opposed to the center frequency that sets the location of the deviation peak because the center frequency would also be altered by the Δka_{eff} value. Lastly, these curves seem to indicate that the location of the deviation peak is not affected by the scatterer size. Although the peak has been shifted to slightly lower frequencies for the 50 μm scatterers, this shift may correspond to a

slight down shift in the backscattered spectrum due to the larger scatterer size. More will be said about the relationship between the peak in the backscattered spectrum and the peak in the deviation later in this section.

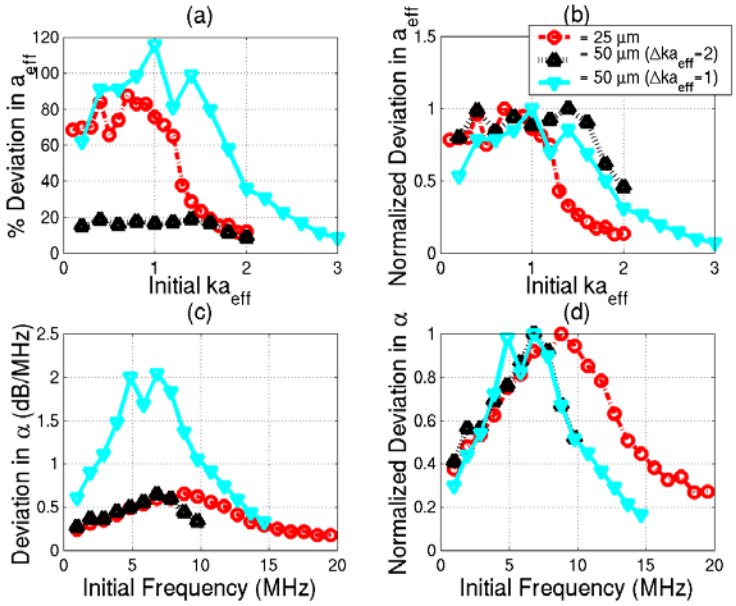

Figure 7.10: Simulation results for different scatterer sizes (25 and 50 µm) for (a) the percent error in the average scatterer size, (b) the percent deviation in the scatterer size, (c) the error in the average total attenuation, and (d) the deviation in the total attenuation plotted versus the initial ka_{eff} value and the initial frequency used in minimization for a Δka_{eff} values of 1 and 2.

After considering the effect of scatterer size on the location of the deviation peak, the location of the peak was investigated to determine if it could be correlated with either the attenuation estimate or the scatterer size estimate individually. Hence, the simulation data for the lossless half-space containing 25 µm scatterers at a density of 35/mm^3 for the source with filtering characteristics given by Equation (7.4) and the Rayleigh source with a σ_R of 18 MHz and a f_R of 8 MHz in the filtering function given by Equation (7.1) were re-analyzed. The analysis was redone twice. First, the algorithm was supplied the correct attenuation and solved only for the scatterer size as was done in Section 7.2. Then, the algorithm was supplied the correct scatterer size and solved only for the attenuation. For both situations, the Δka_{eff} used in the minimization was manually set to 1 while the initial ka_{eff} value was varied over the largest possible range. Once again, a hamming window with a length of 3 mm was used to gate the time domain waveforms. The results for solving for the scatterer size only are given in Figure 7.11 while the results for solving for the attenuation only are given in Figure 7.12.

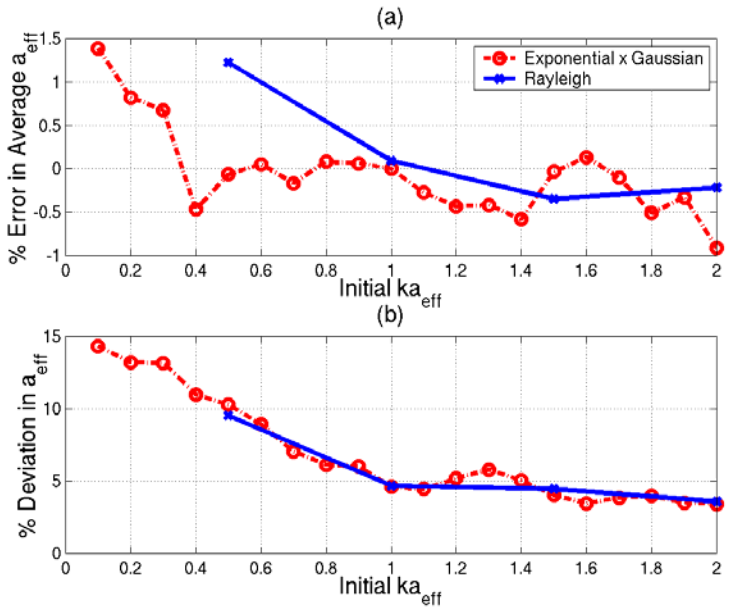

Figure 7.11: Simulation results for different initial ka_{eff} values when α is known (traditional estimation algorithm) for different source filtering functions showing (a) the percent error in the average scatterer size and (b) the percent deviation in the scatterer size.

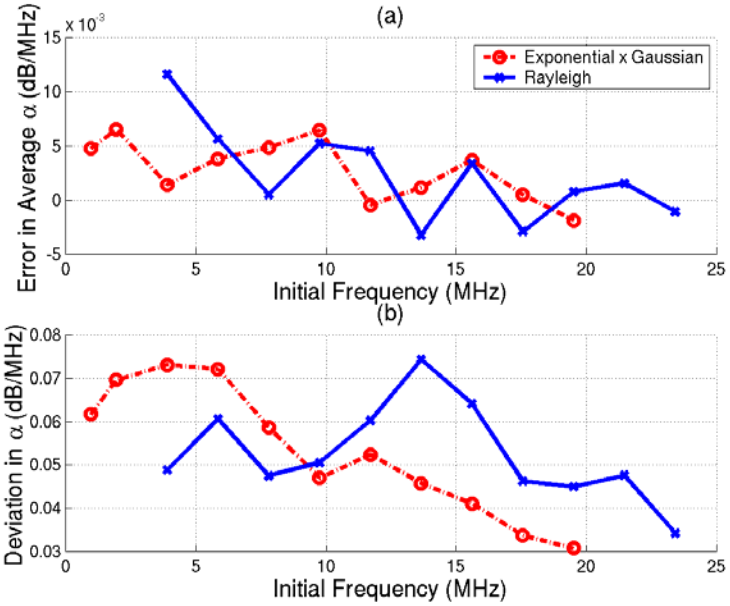

Figure 7.12: Simulation results for different initial ka_{eff} values when a_{eff} is known for different source filtering functions showing (a) the error in the average total attenuation and (b) the deviation in the total attenuation.

When the attenuation is known (i.e., solve only for scatterer size), there is no peak in the deviation of the estimates and the two different sources yield the same accuracy and precision for all of the different initial ka_{eff} values. When the scatterer size is known (i.e., solve only for

attenuation), a slight peak is observable in the deviation. In addition, the location of the peak is different for the two sources considered. However, the locations of the deviation peaks in Figure 7.12b are different from the locations of the corresponding peaks in Figure 7.8d when both scatterer size and attenuation were estimated. In addition, the peak for the source with the Rayleigh distribution has approximately the same value as the peak for the source whose $H(f)$ is given by Equation (7.4), whereas previously (Figure 7.8) the former had a much larger peak value. Also, the precision of the estimates for both sources at smaller initial frequency values (i.e., before the peak) do not overlap whereas before (Figure 7.8) the values of precision were very similar for smaller initial frequencies.

From these observations, it is concluded that the occurrence of the deviation peak cannot be correlated independently with the scatterer size estimate. The occurrence and location of the deviation peak may be related more to the attenuation estimate, but the differences between the results shown in Figures 7.12 and 7.8 would suggest that the peak still cannot be independently correlated with the attenuation estimate. Regardless, the estimation of both parameters tends to enhance the relative maximum value of the deviation peak as well as shift the peak's location to higher values of initial frequency.

The last issue regarding the initial ka_{eff} value that was addressed in this investigation involved determining whether the deviation peak could be observed in "real" sources rather than the artificially large bandwidth sources considered thus far in this section. Hence, some of the previously acquired simulation data for a source with a filtering function given by

$$H(f) = \frac{|f| \cdot \exp\left(-\left(\frac{f - 8\,\text{MHz}}{6\,\text{MHz}}\right)^2\right)}{\max\limits_{\forall f}\left(f \cdot \exp\left(-\left(\frac{f - 8\,\text{MHz}}{6\,\text{MHz}}\right)^2\right)\right)} \tag{7.5}$$

was reanalyzed. In particular, we considered the data for when this source sonified a lossless half-space containing 105 μm scatterers, a lossless half-space containing 55 μm scatterers, and a half-space with an attenuation of 0.5 dB/cm/MHz containing 85 μm scatterers. Once again, the Δka_{eff} used in the minimization was manually set to one, the initial ka_{eff} value was varied over the largest possible range, and a hamming window with a length of 3 mm was used to gate the time domain waveforms. The results for each case are shown in Figure 7.13. Once again, there is a peak in the deviation of the attenuation estimate that is located at a different location for all three

cases corresponding to a plateauing followed by dramatic improvement in precision of the scatterer size estimate. Also, the improvement in the precision of the estimates is also accompanied by an improvement in the accuracy of the estimates confirming that the deviation peak should also occur for a realizable source.

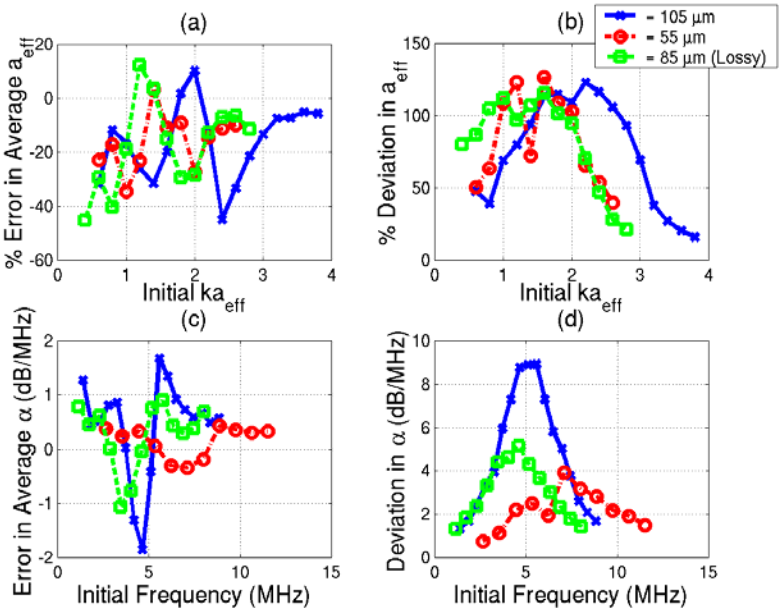

Figure 7.13: Simulation results for realizable source filtering function $H(f)$ for scatterer sizes of 105 μm and a half-space attenuation of 0 dB/cm/MHz, 55 μm and a half-space attenuation of 0 dB/cm/MHz, and 85 μm and a half-space attenuation of 0.5 dB/cm/MHz for (a) the percent error in the average scatterer size, (b) the percent deviation in the scatterer size, (c) the error in the average total attenuation, and (d) the deviation in the total attenuation plotted versus the initial ka_{eff} value and the initial frequency used in minimization for a Δka_{eff} of 1.

At this point, the relationship between the backscattered spectrum and the location of the α deviation peak that was observed throughout the course of the analysis of the initial frequency is summarized in Figure 7.14. In this plot, the ideal backscattered spectrum peak was found by multiplying the reference signal from the rigid plane placed at the focal plane for each source by $k_o^4 \exp\left(-0.827\left(ka_{eff}\right)^2 - 4\alpha z_T\right)$, where a_{eff}, α, and k were the correct values for the scatterer size, attenuation, and wavenumber for the half-space, respectively, and then finding the frequency corresponding to the maximum value. The location of the α deviation peak (i.e., corresponding initial frequency) found for all of the previous cases where both scatterer size and attenuation were estimated was then plotted against each ideal backscattered spectrum peak. The resulting points were then fit by a line that is also shown in Figure 7.14.

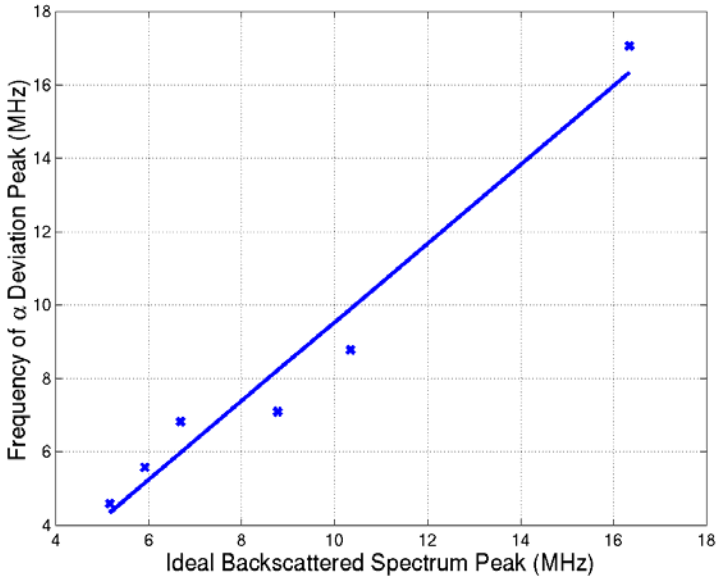

Figure 7.14: Relationship between ideal backscattered spectrum peak and location of a deviation peak for all simulated cases (**x**) shown with linear fit (solid line).

From this figure, it is clear that there is a direct correspondence between the location of the α deviation peak and the ideal backscattered spectrum peak. This correspondence does not seem to be affected by source bandwidth, half-space attenuation, scatterer size, scatterer number density, sampling rate of RF waveforms, or the duration of the frequency range used to perform the minimization. Unfortunately, in the cases considered thus far, the dramatic improvement in precision following the α deviation peak occurs on the trailing edge of the backscattered spectrum that is not usable once electronic noise has been added to the signals. However, it may be possible to design a transmitted spectrum using some type of coding scheme to capitalize on the observed improvement in precision in the future. In addition, although care was taken to insure that the observed α deviation peak was not an artifact of the simulation, future studies should attempt to duplicate the results using real sources and an appropriate tissue model to further confirm that the observed peak is real.

7.4 Chapter Summary

In this chapter, the impact of initial frequency, frequency, initial ka_{eff} value, and Δka_{eff}, on the accuracy and precision of the Spectral Fit algorithm was investigated. The accuracy and precision of the attenuation estimate were consistently improved by increasing the frequency

range while the accuracy and precision of the scatterer size estimate were consistently improved by increasing Δka_{eff}. The improvement observed explained the dependence of precision on half-space attenuation and electronic noise that was observed in Chapter 5. Also, the dependence of the traditional estimation algorithm was investigated and shown to exhibit a similar dependence on Δka_{eff}, and the use of initial ka_{eff} values greater than 0.5 for the traditional algorithm was validated. In addition, the Spectral Fit algorithm was shown to exhibit a peak in the deviation of the attenuation estimate versus initial frequency that was shown to be correlated with the frequency location of the peak in the backscattered spectrum. The occurrence of the deviation peak may be useful in the future to improve the precision if it is not an artifact of the simulation.